J. Astrophys. Astr. (2022)43:23
https://doi.org/10.1007/s12036-022-09804-z

BINARIES

Properties of the accretion disc, jet and disc-wind around Kerr black hole

INDU K. DIHINGIA* and BHARGAV VAIDYA

Department of Astronomy, Astrophysics and Space Engineering, Indian Institute of Technology Indore, Khandwa Road, Simrol 453552, India.
*Corresponding author. E-mail: idihingia@iiti.ac.in

MS received 30 July 2021; accepted 21 December 2021

Abstract. Relativistic jets and disc-winds are energetic phenomena exhibited by various sources, including Active Galactic Nuclei (AGNs) and black hole X-ray binaries (BH-XRBs). Despite recent observational advances in unraveling the region close to the black hole, many aspects of jet launching and particularly the jet-disc connection in these sources are not fully understood. This study investigates the role of the aspect ratio (H/r) of the underlying accretion disc on the jet launching. In this regard, we use an axisymmetric GRMHD framework with adaptive mesh refinement and initialize our simulations with a thin accretion disc in hydro-static equilibrium. In our simulations, we observe Blandford & Znajek (BZ) jet, Blandford & Payne (BP) disc-wind and $B_{\rm tor}$ dominated disc-wind. We find that the aspect ratio of the underlying accretion disc plays a crucial role in the dynamical properties of jet and disc-winds. For an accretion disc with a low aspect ratio, we observe the BZ-jet be thinner and the $B_{\rm tor}$ dominated disc-wind component of the disc-wind to be broader. Further, the BP disc-wind launching radius is closer for an accretion disc with a low aspect ratio. Such a variable launching area of BP disc-wind with an aspect ratio of the underlying disc can have potential implications on understanding the origin of jet dichotomy. Additionally, from the temporal evolution of magnetic flux, we also find the discs with higher aspect ratios are more susceptible to transform into a magnetically arrested disc (MAD) and result in more intermittent wind and jet properties.

Keywords. Accretion—magneto-hydrodynamics—methods:numerical—Galaxies:jets.

1. Introduction

With the increase of sophisticated astronomical observation facilities, developing unified numerical tools is also essential. For the last two decades, general relativistic magneto-hydrodynamical (GRMHD) simulations have been serving as essential tools to understand physics around black holes, and they are helping in understanding accretion physics in great detail (Balbus & Hawley 1998; Han 2017). There are many active GRMHD simulation codes available in the literature, and they provide comparatively similar results (Porth *et al.* 2019). Although due to lack of unification, there are still discrepancies between observational findings from active galactic nuclei (AGNs) as well as black hole X-ray binaries (BH-XRBs) and theoretical/numerical predictions for the same (Davis & Tchekhovskoy 2020).

Astrophysical jets are very commonly observed in many astrophysical systems, viz. young stellar objects, BH-XRBs, gamma-ray bursts (GRBs), and AGNs (see Fernandes *et al.* 2012; Fender & Gallo 2014; Davis & Tchekhovskoy 2020). There are two primary mechanisms dealing with launching astrophysical jets, namely, Blandford & Znajeck (BZ) and Blandford & Payne (BP, disc-wind) mechanism (Blandford & Znajek 1977; Blandford & Payne 1982; Komissarov 2004).

Most of the GRMHD simulations rely on the initial hydrostatic torus at equilibrium (Fishbone & Moncrief 1976). Such simulations are well equipped to study physics near the event horizon. Numerous studies have been performed using 2D and 3D simulations to understand the launching of the BZ jet using torus

This article is part of the Special Issue on "Astrophysical Jets and Observational Facilities: A National Perspective".

Published online: 28 April 2022

setups. It has been shown that the accretion process around the Kerr black hole is well correlated with the spin parameter of the black hole (De Villiers & Hawley 2003). Also, it has been demonstrated that the BZ jet extracts energy from the Kerr black hole and the jet power increases roughly as a square of the Kerr parameter (McKinney & Gammie 2004; Tchekhovskoy *et al.* 2010, 2011; Narayan & McClintock 2012). This property is particularly important and handy in the continuum fitting method to determine the Kerr parameter of black hole sources (see Zhang *et al.* 1997; McClintock *et al.* 2006; You *et al.* 2016; Reynolds 2019).

With the development of general relativistic ray-tracing codes, GRMHD simulations are now efficient tools to study the emission properties from the accretion disc (Noble *et al.* 2011; McKinney *et al.* 2014; Dexter 2016; Younsi *et al.* 2016; Bronzwaer *et al.* 2018, 2020; Chatterjee *et al.* 2020b; Mościbrodzka 2020). Simulations have suggested the formation of plasmoids due to the reconnection of the field lines (Nathanail *et al.* 2019, 2020; Porth *et al.* 2019). Plasmoids are viable candidates to understand the non-thermal radiations as well as the observed flaring activities in astrophysical sources (Chatterjee *et al.* 2020a; Dexter *et al.* 2020; Ripperda *et al.* 2020; Porth *et al.* 2021).

Very-long-baseline interferometry (VLBI) observations of astrophysical jets suggest that the jet launching radius for M87 is about $\sim 5.5R_g$, where R_g is the Schwarzchild radius (Doeleman *et al.* 2012; Kim *et al.* 2018; Nakamura *et al.* 2018). This observation indicates that the jet of M87 is launched from close to the innermost stable circular orbit (ISCO). The responsible jet launching mechanism is probably the BZ process in the case of the M87 jet. On the other hand jet launching radius for Cyg A is found to be $\sim 227R_g$ (Boccardi *et al.* 2016). This investigation suggests that at least a part of the jet is launched very far from the black hole for Cyg A, possibly due to the BP process. Thus it is often believed that in realistic scenarios, both BZ and BP processes act concurrently in launching the astrophysical jet (Hardee *et al.* 2007; Xie *et al.* 2012).

In order to study the combined effect of BZ-jet and disc-wind, GRMHD simulations with a thin disc at equilibrium are essential. Earlier, with 2D GRMHD thin-disc simulations, Qian *et al.* (2018), Vourellis *et al.* (2019) have shown the simultaneous presence of BZ-jet and disc-wind. In their simulations, disc-wind is primarily by toroidal dominated component. The launching mechanism of the toroidal dominated disc-wind is the gradient of magnetic pressure. Recently, Dihingia *et al.* (2021) have shown the presence of BP-driven disc-wind for a strong inclined magnetic field structure. They have not studied the dependencies of the aspect ratio (H/r) of the accretion disc on launching jet and disc-winds. In general, depending on the disc aspect ratio (H/r), the physical nature of the accretion can be different (Yuan & Narayan 2014). An earlier parametric study by Tchekhovskoy *et al.* (2010) also hinted at the possible link of disc aspect ratio with the radio-loud/quiet dichotomy of AGN jets. Thus, the aspect ratio of the accretion disc may play a crucial role in the dynamical properties of the accretion-ejection system. Also, it may affect the launching mechanism of the disc-winds. A careful and rigorous study is required to understand the essence of the aspect ratio. In this work, we investigate the influences of aspect ratio on the accretion-ejection system. Nevertheless, in this study, we will be investigating the properties of the jets and disc-winds only in the geometrically thin regime.

This study is organized as follows. Section 2 describes our model setup, including the essential mathematical background, the initial setup, and the parametric models. Subsequently, Section 3 describes our results, explaining BZ-jet, disc-wind, and comparison of findings obtained from different models. Finally, Section 4 presents the conclusions based on Section 3 and summarizes the study with a discussion.

2. Model setup

The ideal GRMHD equations are expressed in terms of the rest-mass density (ρ), the fluid four velocities (u^μ), the energy-momentum tensor ($T^{\mu\nu}$), and the dual of the Faraday tensor ($^*F^{\mu\nu}$) in covariant notation as follows:

$$\nabla_\mu(\rho u^\mu) = 0, \quad \nabla_\mu T^{\mu\nu} = 0 \quad \text{and} \quad \nabla_\mu {}^*F^{\mu\nu} = 0. \tag{1}$$

These equations correspond to mass conservation, energy-momentum conservation, and homogeneous Faraday's law, respectively. We adopt `code BHAC` (Porth *et al.* 2017; Olivares *et al.* 2019) to solve these sets of equations in 2.5D, i.e., we consider the flow to have axial symmetry, and solve these set of equations in 2 spatial directions (r, θ) in Modified Kerr–Schild (MKS) geometry. The simulation domain is extended in the angular direction from $\theta = 0 \rightarrow \pi$. Whereas, in the radial direction, the simulation domain is extended

Table 1. The explicit values of effective resolution, and Θ_0, and maximum aspect ratio $(H/r)_{\max}$ for different simulation models.

Model	Effective resolution	Θ_0	$(H/r)_{\max}$
A	1024×512	0.005	0.16
B	1024×512	0.001	0.07
C	1024×512	0.0001	0.02

up to $r_{\text{out}} = 500$. We express all the quantities in a normalized unit system with G (universal gravitational constant) $= M_{\text{BH}}$ (mass of the black hole) $= c$ (speed of light) $= 1$. For example, in this unit system, time is expressed in terms of GM_{BH}/c^3.

We set up a initial thin-disc following Dihingia *et al.* (2021) (DVF setup), the setup is based on the Novikov & Thorne (1973) model. DVF setup is characterised in terms of Kerr parameter $a_{\mathcal{K}} = 0.9375$, entropy constant $\mathcal{K} = 0.1$, polytropic index $\Gamma = 4/3$, initial maximum plasma-β parameter $\beta_{\max} = 500$, and inclination parameter of the initial poloidal magnetic field $m = 0.1$. Note that the structure of the initial poloidal magnetic field is incorporated following Zanni *et al.* (2007). Here, $\beta_{\max} = p_{\text{gas}}^{\max}/p_{\text{mag}}^{\max}$ and the maximum of gas pressure and magnetic pressures are obtained at the density maximum of the thin disc $(r = 2.9797)$. Depending on our motivation, we devised three simulation models with $\Theta_0 = 0.005$, 0.001, and 0.0001, where Θ_0 is a constant that determines the accretion disc's initial disc height. The Θ_0 essentially governs the maximum temperature of the initial accretion disc. The detail of these models is given in Table 1. For the sake of illustration and comparison, we consider model B to be our reference model.

In Figure 1, we show the initial density profile for different simulation models A, B, and C, in panels (a), (b), and (c), respectively. In our simulations, we do not consider any radiative cooling and explicit viscous heating. In reality, a thin disc is known to be radiatively efficient (Shakura & Sunyaev 1973). However, due to local heat balance conditions in the thin disc, the contribution from these physical processes is minimum in the dynamical behaviors of the accretion disc (see Shakura & Sunyaev 1973; Paczynski & Bisnovatyi-Kogan 1981, etc.). Therefore, in the hydrodynamical limit $(B^i \sim 0)$, the DVF setup does not suffer significant changes with temporal evolution (Dihingia *et al.* 2021).

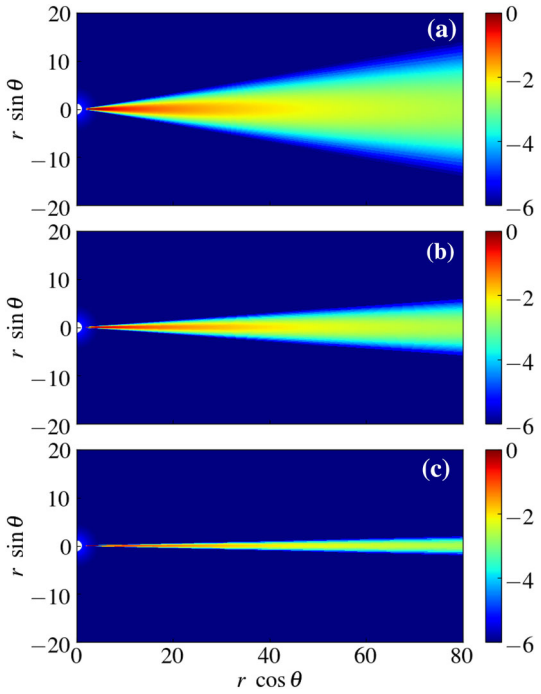

Figure 1. Distribution of initial normalized logarithmic density profile $(\rho/\rho_{\max})$ on the poloidal plane for models (a) A, (b) B, and (c) C.

3. Results

In this section, we present the results obtained from our different simulation models. In Figure 2, we show the temporal evolution of the logarithmic density profile $(\rho/\rho_{\max})$ for reference model at time $t = 500$, 1000, 2000, and 3000 (left to right). In the figure, black solid line corresponds to the magnetisation $\sigma = b^2/\rho = 1$ contour.

As we start our simulation runs, the toroidal motion of the flow winds up supplied poloidal magnetic field. It generates the toroidal component (B_{tor}) of the magnetic field. Subsequently, the magnetic field helps transport angular momentum outside (see Dihingia *et al.* (2021) for detailed discussion). The transport of angular momentum depends on the resolved magneto-rotational instabilities (MRI) in our simulations. The transport of angular momentum essentially sets the accretion of matter. As a result, the flow in the high-density initial thin disc distributes into different components. Finally, the simulation reaches a quasi-steady state after a certain simulation time with three major components, viz., (i) high-density thin disc, (ii) very-low-density funnel region (BZ-jet, area under $\sigma = 1$ contour), and (iii) low-density disc-wind.

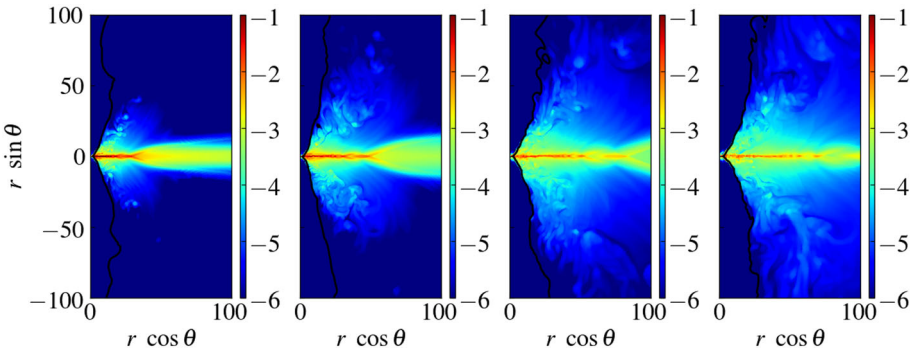

Figure 2. Temporal snapshots of the logarithmic density distribution $(\rho/\rho_{\rm max})$ on the poloidal plane for reference model at time $t = 500$, 1000, 2000, and 3000, respectively. Black solid line corresponds to $\sigma = 1$ contour.

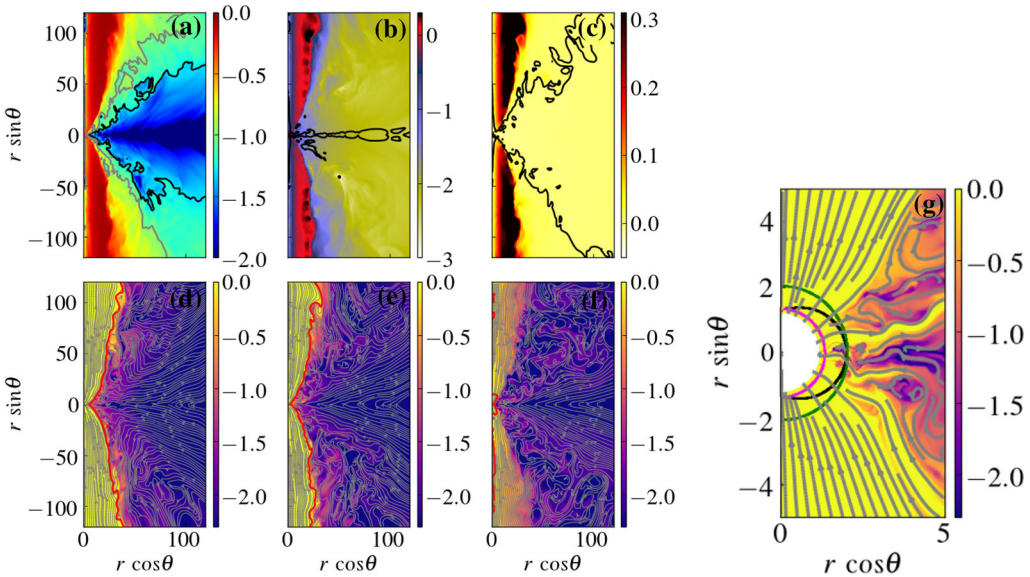

Figure 3. Logarithmic distribution of (a) vertical velocity $(|v_z|)$, (b) Lorentz factor $(\gamma - 1)$, (c) Bernoulli parameter $(-hu_t)$ for reference model, magnetisation (σ) for model (d) A, (e) B, and (f) C is shown at simulation time $t = 3000$. In panel (g), inner part of (e) is shown. See text for more details.

Below, we discuss the properties of these different regions in detail. Also, compare the results between different simulation models to understand the impact of the aspect ratio in launching jet and disc-wind.

3.1 *BZ-jet*

BZ-jet is very commonly observed in GRMHD simulations. The launching of BZ-jet with DVF setup is extensively studied by Dihingia *et al.* (2021). The properties of BZ-jet is shown for reference model (model B) in panels (a), (b), and (c) of Figure 3 at a simulation time $t = 3000$. In panel (a), the distribution of the logarithmic vertical velocity $(|v_z|)$ is shown, where the black and grey lines correspond to $|v_z| =$ 0.05 and 0.1 contours, respectively. In panel (b), we show the distribution of logarithmic Lorentz factor in terms of $(\gamma - 1)$, where black line corresponds to the contour of $u^r = 0$. Finally, in panel (c), we show the logarithmic distribution Bernoulli parameter $(-hu_t)$, where black line corresponds to $-hu_t = 1$ contours. Additionally, to study the launching of BZ-jet from accretion disc with different aspect ratios, we show the distribution of logarithmic magnetization (σ) at time $t = 3000$ along with the magnetic field lines for models A, B, and C in panels (d), (e), and (f) of Figure 3, respectively. The red contours in the panels (d), (e), and (f) corresponds to the $\sigma = 1$. In the panel Figure 3(g), we have shown the inner part of the Figure 3(e), also drawn three semicircles depicting the event horizon (magenta), ergosphere (black), and the radius of ISCO (green).

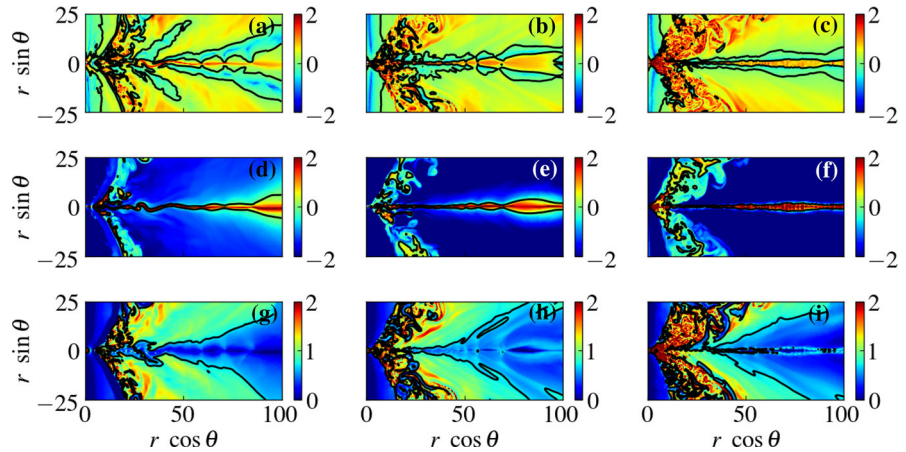

Figure 4. Distribution of logarithmic Alfvénic Mach number ($M_{\rm A,P}$) (upper row), plasma-β (middle row) and $B_{\rm tor}/B_{\rm p}$ (lower row) for models A (left column), B (middle column), and C (right column) at a simulation time $t = 3000$. Solid black contours corresponds to $M_{\rm A,P} = 1$ (upper row), $\beta = 1$ (middle row), and $B_{\rm tor}/B_{\rm p} = 5$ (lower row).

In the low-density funnel region, flow is highly relativistic $|v_z| \sim 1$, Lorentz factor $\gamma \sim 10$, gravitationally unbound $(-hu_t > 1)$, and highly magnetized $(\sigma > 1)$. We also observe poloidal magnetic field lines rooted to the ergosphere of the black hole (see Figure 3g). These facts strongly suggest the presence of active BZ-jet in our simulations (Blandford & Znajek 1977; Komissarov & Barkov 2009). By comparing the results from different models, we find that the BZ-jet appears thinner for thinner accretion disc (lower aspect ratio). Also, the BZ-jet (or funnel region) is less magnetized for accretion disc with a low aspect ratio (see Figure 3d, e, and f). Thus vertical velocity and Lorentz factor of the BZ-jet decreases as the aspect ratio of the disc decreases.

3.2 *Disc-wind*

Disc-wind from accretion disc around black holes comes in two flavors, $B_{\rm tor}$ dominated and BP dominated. In order to study the affect of disc-heights on disc-wind we show the distribution of Alfvénic Mach number ($M_{\rm A,P}$) (upper row, (a), (b), and (c)), plasma-β (middle row, (d), (e), and (f)), and ratio $B_{\rm tor}/B_{\rm p}$ (lower row, (g), (h), and (i)) for models A (left column), B (middle column), and C (right column) in Figure 4 at a simulation time $t = 3000$. We obtain poloidal Alfvénic Mach number as $M_{\rm A,p} = u_{\rm p}/c_a$, where

$$h = 1 + \frac{\Gamma p}{(\Gamma - 1)\rho}, \quad c_a^2 = \frac{B_{\rm p}^2}{(\rho h + B_{\rm p}^2)},$$
$$u_{\rm p}^2 = [u^r u_r + u^\theta u_\theta]_{\rm BL}$$

and finally $B_{\rm p}^2 = [B^r B_r + B^\theta B_\theta]_{\rm BL}$. Subsequently, the toroidal component of the magnetic fields are calculated as $B_{\rm tor}^2 = [B^\phi B_\phi]_{\rm BL}$. Quantities with subscript BL[1] are calculated in Boyer–Lindquist coordinates. The solid black contours corresponds to $M_{\rm A,P} = 1$ (upper row), $\beta = 1$ (middle row), and $B_{\rm tor}/B_{\rm p} = 5$ (lower row).

In the reference model (middle column of Figure 4), closer to the black hole $r \lesssim 10$, the disc-wind launches with $B_{\rm tor}/B_{\rm p} > 5$ and with super-Alfvénic velocity $(M_{\rm A,P}) > 1$. Essentially suggests that the disk matter are lunched to the disc-wind from the underlying surface of the accretion disc due to the gradient of strong toroidal magnetic pressure. This component of the disc-wind is known as $B_{\rm tor}$ dominated wind. Whereas, for $r \gtrsim 10$, the disc-wind is sub-Alfvénic while leaving the disc surface. The disc-wind makes a transition from sub-Alfvénic to super-Alfvénic as it moves far from the disc surface. Inside the thin disc, the flow is super-Alfvénic, and the ratio of the magnetic field components $B_{\rm tor}/B_{\rm p} \lesssim 1$ (see dark green color in Figure 4f). The ratio $B_{\rm tor}/B_{\rm p}$ also increases as the disc-wind moves far from the disc surface. Interestingly, the thin disc remains gas pressure dominated (see the middle row of Figure 4), and at the disc-surface magnetic pressure started to dominate. These facts strongly suggest that the disc-wind is magnetically driven due to magneto-centrifugal acceleration. This component of the disc-wind is commonly known as BP disc-wind (Blandford & Payne 1982). We define the minimum radius beyond which we observe BP-driven disc-wind as BP launching radius ($r_{\rm BP}$). Note that in this case, the BP launching radius $r_{\rm BP} \sim 10$.

[1]The value of $u_{\rm p}^2$ and $B_{\rm p}^2$ depends on the coordinates. We calculate them in Boyer–Lindquist coordinates, as it is the physical coordinate system of black hole.

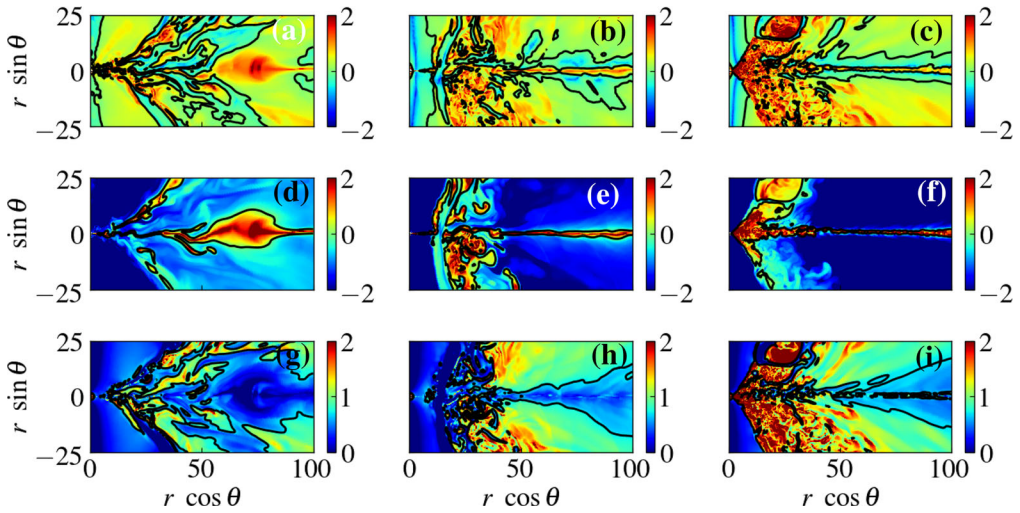

Figure 5. Distribution of logarithmic Alfvénic Mach number ($M_{A,P}$) (upper row), plasma-β (middle row), and B_{tor}/B_p (lower row) for models A (left column), B (middle column), and C (right column) at a simulation time t = 7500 . Black contours corresponds to $M_{A,P} = 1$ (upper row), $\beta = 1$ (middle row), and $B_{tor}/B_p = 5$ (lower row).

The disc-wind initially launched with very small vertical velocity from the surface of the disc (see Figure 3a). As the wind moves far from the disc equatorial plane, it accelerates, and the vertical velocity increases. Finally, after moving a certain distance from the equatorial plane, the winds become gravitationally unbound ($-hu_t > 1$, see Figure 3c). In that region, even for BP disc-wind also, toroidal component dominate and aide to the self collimation of the disc-wind (Blandford & Payne 1982; Fendt 2006, and references therein). The disc-wind surrounds the fast BZ-jet in a spine-sheath structure. That makes the disc-wind a key driver of maintaining the large-scale structure of the jet.

Comparing panels of Figure 4, we investigate the properties of the disc-wind for thin ($\Theta_0 = 0.005$, high aspect ratio), thinner ($\Theta_0 = 0.001$, moderate aspect ratio), and thinnest ($\Theta_0 = 0.0001$, low aspect ratio) accretion disc. As the aspect ratio of the accretion disc reduces, the initial magnetic flux (poloidal) within the disc reduces. In such a weakly magnetized accretion disc, MRI can efficiently destabilize the rotating matters and drive turbulence. Eventually, the MRI turbulence amplifies the toroidal magnetic field component (Begelman & Pringle 2007). Thus in an accretion disc with a low aspect ratio, the toroidal component generates efficiently. Essentially results in a wider B_{tor} dominated disc-wind for such an accretion disc. Essentially suggest that the disc-wind launched from such an accretion disc is more turbulent. Such turbulent disc-wind are prone to reconnection events. It is noteworthy that reconnection events lead to the formation of plasmoids, and they are ideal sites for particle acceleration (Begelman *et al.* 1990; Stecker *et al.* 1991; Alvarez-Muñiz & Mészáros 2004; Sironi *et al.* 2015; Inoue *et al.* 2019). On the other hand, for a model with higher magnetic flux (model A), the MRI-driven turbulence is suppressed due to the presence of a strong magnetic field (Bonanno & Urpin 2008). In such cases, instabilities like magnetic–Rayleigh–Taylor instabilities (MRTI) drive turbulence in the accretion flow (Igumenshchev 2008; Avara *et al.* 2016; Marshall *et al.* 2018). MRTI destabilized flow very near to the black hole, which leads to thinner B_{tor} dominated the disc-wind. Since turbulence cannot destabilize the poloidal component, it shows a prominent BP-driven disc-wind than other models (B and C).

Also, a low aspect ratio accretion disc essentially means a cooler accretion disc (low Θ_0). That significantly affects the long-term dynamics of the disc wind. In Figure 5, we show the profiles of Figure 4 at a later time t = 7500. We observe that the signature of BP-driven disc-wind reduces for models with a high aspect ratio (see the first column of Figure 5). The value of plasma-β increases near the disc surface up to the order of $\beta \sim 0.1$. As the comparatively hotter equatorial matter spreads to the off-equatorial part. The launching radius of BP-driven wind pushes outside with simulation time. For model A, the BP launching radius is about $r_{BP} \sim 20$ at $t = 3000$, and $r_{BP} \sim 90$ at time t = 7500. For model B, the BP launching radius is about $r_{BP} \sim 10$ at $t = 3000$, and $r_{BP} \sim 40$ at time t = 7500. On the other hand, for

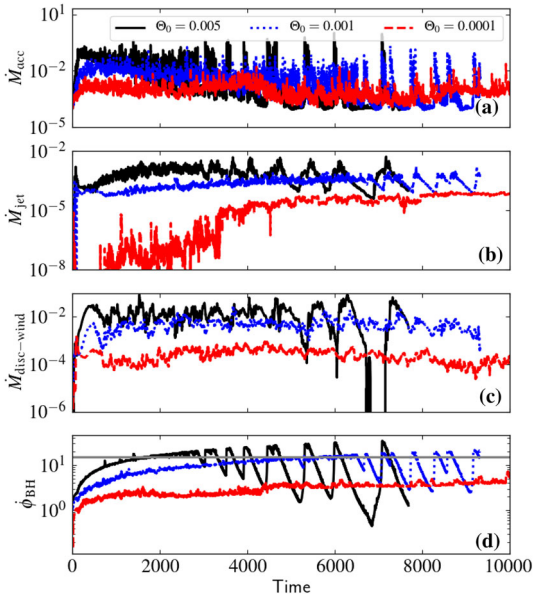

Figure 6. Plot of accretion rate ($\dot{M}_{\rm acc}$), jet rate ($\dot{M}_{\rm jet}$), wind rate ($\dot{M}_{\rm disc-wind}$), and magnetic fluxes($\dot{\phi}_{\rm BH}$) with simulation time. The horizontal line in panel (d) corresponds to $\dot{\phi}_{\rm BH} = 15$. Solid black, dotted blue, and dashed red lines corresponds to models A ($\Theta_0 = 0.005$), B ($\Theta_0 = 0.001$), and C ($\Theta_0 = 0.0001$), respectively.

model C (thinnest one), equatorial matters are sufficiently cooler it does not increase the value of plasma-β, it remains in the order of $\beta \sim 0.01$. Thus for model C, the BP-driven wind remains there throughout the temporal domain of simulation. Also, the launching radius of BP-driven wind remains smaller for model C. For model C, the BP launching radius is about $r_{\rm BP} \sim 10$ at $t = 3000$ and $r_{\rm BP} \sim 20$ at time t = 7500.

3.3 *Time series*

In this section, we study the temporal evolution of mass flux rates through different regions, and magnetic flux rates calculated following Porth *et al.* (2017); Dihingia *et al.* (2021). In the panels (a), (b), (c), and (d) of Figure 6, we show accretion rate $\dot{M}_{\rm acc}$, jet rate $\dot{M}_{\rm jet}$, disc-wind rate $\dot{M}_{\rm disc-wind}$, magnetic flux $\dot{\phi}_{\rm BH}$, respectively, as function of simulation time for different models.

Due to the turbulence generated by MRI, the angular momentum transported outwards essentially sets a very small negative radial velocity ($u^r \lesssim 0$) in the thin disc (see Figure 3b). That triggers disc-wind in the system. Subsequently, disc-winds also take away angular momentum along with it, which increases the accretion rate and disc-wind rate (Dihingia *et al.* 2021). Finally, after a certain simulation time, all models reach to quasi-steady state. The time required to reach a quasi-steady state is different for different models.

With the decrease of the aspect ratio of the initial disc (model A $\rightarrow$ C), $B_{\rm tor}$ disc-wind is more prominent. In this situation, the angular momentum is transported primarily due to $B_{\rm tor}$ disc-wind. However, for higher aspect ratio cases, along with $B_{\rm tor}$ disc-wind, large-scale magnetic stress also transports angular momentum through BP disc-wind. As a result, we observe a lower quasi-steady value of accretion rate ($\dot{M}_{\rm acc}$) for low aspect ratio accretion disc cases as compared to high aspect ratio accretion disc. Subsequently, a similar trend is followed by the mass flux rate through the jet ($\dot{M}_{\rm jet}$) and disc-wind ($\dot{M}_{\rm disc-wind}$).

With temporal evolution, magnetic flux ($\dot{\phi}_{\rm BH}$) started to accumulate around the event horizon. Due to flux freezing conditions, we expect a faster accumulation of magnetic flux for higher accretion cases. Consequently, models with a higher aspect ratio accumulate magnetic flux faster as compared to a model with a lower aspect ratio. Therefore, disc-thickness plays a decisive role in determining when the accretion disc attains a magnetically arrested disc (MAD) configuration. In order to achieve a MAD configuration, the magnetic flux accumulation rates ($\dot{\phi}_{\rm BH}$) need to have a value of the order of $\dot{\phi}_{\rm BH} \sim 15$ (see the horizontal line in Figure 6d) (Tchekhovskoy *et al.* 2011). In Figure 6(d), we observe that model A reaches to MAD configuration faster compare to model B. However, model C remains in SANE (standard and normal evolution) configuration, and it does not reach a MAD configuration within the temporal domain of our simulation. Note that how soon a model reaches to MAD configuration also depends on the strength of the initial magnetic field (Dihingia *et al.* 2021). In general, the jet power increases with the magnetic flux and mass flux rate through the funnel region (Blandford & Znajek 1977; Tchekhovskoy *et al.* 2011). Consequently, the model with a higher aspect ratio will have higher jet power than a model with a lower aspect ratio.

After a sufficiently long time, we observe that the accretion rate ($\dot{M}_{\rm acc}$) started to oscillate (see Figure 6). The oscillation in model A starts at $t \sim 3000$, whereas in model B, oscillation starts at $t \sim 7000$. On the contrary, we do not observe any oscillations in model C within our simulation time domain. These oscillations are closely related to the reconnection events

happening near to black hole. The plasmoids formed due to the reconnection events advects with the disc-wind leaving newly reconnected poloidal magnetic fields. That enhanced the magnetic tension force in the inner part of the accretion disc. Eventually, it results in truncation and oscillation of the accretion disc, and the effect of the oscillation can be visible in the mass flux rates as well (see Dihingia *et al.* (2021) for more discussion).

It is evident from Figure 6(d) that the oscillation in the inner part of the disc starts once the accretion flow of the inner part reaches a MAD configuration. In MAD, magnetic tension force becomes strong enough to halt the accretion momentarily. As accretion restarts, MAD significantly loses its magnetic flux leading to magnetic eruptions events. These kinds of magnetic eruption events are often seen in 2D and 3D GRMHD simulations and are particularly important to explain flares from astrophysical sources (Ripperda *et al.* 2020; Chatterjee *et al.* 2020a; Dexter *et al.* 2020; Porth *et al.* 2021).

4. Astrophysical context

It is interesting to note that the simulation models show different qualitative features (MAD/SANE) depending on their aspect ratios despite the same value of $\beta_{\rm max}$. The low aspect ratio disc remains in the SANE configuration. However, higher aspect ratio discs evolve to a MAD configuration (model A and B). In general, the funnel region is broader for MAD configuration in comparison to the SANE configuration (Penna *et al.* 2013; Sádowski *et al.* 2013; Gold *et al.* 2017). Recent polarised image of Event Horizon Telescope Collaboration (EHTC) observation suggests that the accretion flow around M87 is likely to be in MAD configuration (Akiyama *et al.* 2021). However, a detailed polarised radiative transfer modeling of 3D GRMHD simulations is required to discern the nature of the underlying disc for M87. Nevertheless, the present simulations can potentially constrain the accretion disc around M87 to be a high aspect ratio disc, which is prone to transform to a MAD configuration.

Interestingly, we find that the disc aspect ratio significantly affects the spine-sheath structure of the astrophysical jet. To display the spine-sheath structure of our simulation runs, we show the vertical velocity (logarithmic distribution) ($|v_z|$) and magnetic field lines (in gray) for models B and C at time $t = 7500$ in Figure 7. The BZ-jet for accretion disc with a lower

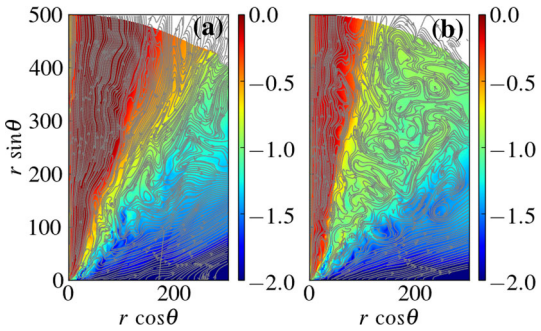

Figure 7. Logarithmic distribution of vertical velocity ($|v_z|$) on the poloidal plane for models B and C at simulation time $t = 7500$.

aspect ratio is thinner and surrounded by a wide turbulent $B_{\rm tor}$ disc-wind, which is surrounded by ordered BP disc-wind. The BZ-jet has a vertical velocity of the order of $v_z \sim 0.87$, Lorentz factor $\gamma \sim 2$, and the power of the jet is comparatively lower. However, the scenario is quite the opposite for the models with high aspect ratios (models A and B). The BZ-jet is wider and surrounded by a very thin $B_{\rm tor}$ disc-wind. The BZ-jet has a vertical velocity of the order of $v_z \sim 0.98 - 99$, Lorentz factor $\gamma \sim 5 - 10$, and the power of the jet is comparatively higher. It essentially suggests that the jet-sheath structure plays a crucial role in the confinement and collimation of the jet spine. The toroidal magnetic field surrounding the BZ-jet is thought to be an essential key ingredient for acceleration and self-collimation of the jet (see Spruit *et al.* (1997); Fendt (2006), for discussion). Note that the self-collimation of the jet within the launching region may not be enough to conclude about the degree of collimation of the astrophysical jets on a large scale. The interaction of the jet with the ambient medium may become essential to understand the large-scale structure of the jet (Tomimatsu 1994; Beskin *et al.* 1998; Komissarov *et al.* 2007; Lyubarsky 2009).

Depending on the large-scale morphology of the hosted jet, there are two classes of galaxies, viz. FR-I and FR-II (Fanaroff & Riley 1974). Its origin is widely discussed in the literature, and it is mainly attributed to the properties of the central host and environmental conditions of the host (Wold *et al.* 2007; Gendre *et al.* 2013; Tchekhovskoy & Bromberg 2016; Mingo *et al.* 2019). The disc-wind creates the initial environment through which a jet initially travels and develops the large-scale structure. Thus disc-wind may provide crucial information about the origin of FR dichotomy (see Boccardi *et al.* (2021) for discussion). Our study also suggests that due to the different structures of

Table 2. The comparative properties of disc, jet, and disc-winds for different aspect ratios. The first, second, and third columns represent different regions, properties for higher and lower aspect ratios, respectively.

Regions	Higher H/r	Lower H/r
Accretion disc	Higher $\dot{M}_{\rm acc}$ (MAD)	Lower $\dot{M}_{\rm acc}$ (SANE)
BZ-jet	Broad, fast, powerful, and highly-magnetised	Thin, slow, less-powerful, and less-magnetised
$B_{\rm tor}$ wind	Thin and less turbulent	Broad, turbulent, and plasmoids seen
BP disc-wind	Larger $r_{\rm BP}$	Smaller $r_{\rm BP}$

spine-sheath, the accretion disc with different aspect ratios provides astrophysical jets in two different doctrines. In one case (low aspect ratio), the jet is thin and less relativistic with less jet power. On the contrary, the jet is wide and highly relativistic with high jet power in another case (high aspect ratio). Consequently, our findings may provide more information about the accretion disc of FR-I and FR-II galaxies. However, a study with proper electron-ion thermodynamics (heating and cooling) would be more robust to infer radiative properties of different classes of galaxies. Incorporation and application of such two-temperature models within the GRMHD simulations are currently under development (Ressler *et al.* 2015; Ryan *et al.* 2017; Sádowski *et al.* 2017; Mizuno *et al.* 2021; etc.).

5. Discussion and summary

In this work, we set up a highly resolved, axisymmetric, magnetized, thin accretion disc following DVF setup (Dihingia *et al.* 2021). With this setup, we investigate the launching of jets, disc-winds from the underlying accretion disc. We extensively studied the influence of the disc aspect ratios on the dynamical behavior of the disc, jet, and disc-wind. The key findings of the present work can be encapsulated as shown in the table. We can identify three distinct regions from our simulation runs: high-density thin accretion disc, slowly moving disc-wind, and low-density fast-moving relativistic jet in the funnel region. Moreover, depending on the launching mechanisms, disc-winds can be divided into two types, $B_{\rm tor}$ dominated and BP dominated disc-wind. The gradient of toroidal magnetic pressure is responsible for $B_{\rm tor}$ dominated disc-wind, whereas magneto-centrifugal acceleration is responsible for BP dominated disc-wind. Disc-wind launches with a very small velocity from the disc surface and accelerates as it moves far from the disc surface. We also find ample evidence for active BZ-mechanism that launches the relativistic jets in the funnel region. These findings confirm the accretion-ejection structure studied by Dihingia *et al.* (2021). The comparative results for these components concerning different aspect ratios are shown in Table 2.

Our simulations also have implications for the FR-dichotomy of galaxies. A recent study suggests that the disc-wind structure is closely related to the origin of the FR dichotomy of galaxies (Boccardi *et al.* 2021). We find that the disc-wind structure depends on the aspect ratio of the accretion disc hosting the jet. Our study hints that the FR dichotomy of galaxies may be closely associated with the structure of the accretion disc itself. However, a 3D GRMHD study will be ideal for inferring more detail about these connections.

In summary, the present work discusses properties of relativistic BZ-jet and disc-wind hosted by thin accretion disc around the Kerr black hole. The models with a higher aspect ratio show a wider BZ-jet and stronger disc-wind. The BP-driven disc-wind for models with a higher aspect ratio shows prominent features initially. With time the launching radius of BP disc-wind increases. However, for models with a lower aspect ratio, the launching radius of BP disc-wind remains close to the black hole ($r_{\rm BP} \sim 20-25$). Thus, the BP disc-wind for accretion disc with a higher aspect ratio can not sustain for a longer time or sustain far from the black hole. In such a situation, the launching of disc-wind is mainly driven by the gradient of toroidal magnetic pressure and gradient of thermal pressure. The inclusion of radiative cooling may become important for models with higher aspect ratios. With significant cooling, the jet launching radius may sustain close to the black hole. Such a study can not be accommodated with the current framework. Finally, we suggest that the structure of the accretion disc may interplay crucial roles in understanding the FR-I and FR-II dichotomy of galaxies. Additionally, the spin of the central black hole will also influence powering of the jet. With parametric consideration of disc, Tchekhovskoy *et al.*

(2010) also suggests that with the increase of disc thickness, the power-law dependence of the jet power on the angular momentum of the black hole becomes much steeper. It will be interesting to investigate the connection between the spin and jet power with an underlying and evolving accretion disc of varying aspect ratios using global GRMHD simulations, which we plan for future studies.

Interestingly, the reconnection zones (plasmoids) in our simulations can have fascinating applications in understanding high energy radiations due to particle acceleration in these sites (Sironi & Spitkovsky 2014; Kagan *et al.* 2015; Sironi *et al.* 2015). These sites are also a potential candidate to provide high-energy neutrinos via hadronic process (Begelman *et al.* 1990; Stecker *et al.* 1991; Alvarez-Muñiz & Mészáros 2004; Sironi *et al.* 2015; Inoue *et al.* 2019). Throughout our study, we consider ideal GRMHD. Thus the reconnection phenomena arising in our simulation is due to numerical resistivity dependent on the resolution of the grids. Relaxing the ideal GRMHD constraint is an endeavor we would like to explore in the future.

Acknowledgments

The authors would like to thank the anonymous referee for the helpful comments, and constructive remarks on this manuscript. All simulations were performed on the Max Planck Gesellschaft (MPG) super-computing resources. Also, they would like to thank the financial support from the Max Planck partner group award at the Indian Institute of Technology of Indore.

References

Akiyama K., *et al.* 2021, Astrophys. J. Lett., 910, L13
Alvarez-Muñiz J., Mészáros P. 2004, Phys. Rev. D, 70, 123001
Avara M. J., McKinney J. C., Reynolds C. S. 2016, MNRAS, 462, 636
Balbus S. A., Hawley J. F. 1998, Reviews of Modern Physics, 70, 1
Begelman M. C., Pringle J. E. 2007, MNRAS, 375, 1070
Begelman M. C., Rudak B., Sikora M. 1990, ApJ, 362, 38
Beskin V. S., Kuznetsova I. V., Rafikov R. R. 1998, MNRAS, 299, 341
Blandford R. D., Znajek R. L. 1977, MNRAS, 179, 433
Blandford R. D., Payne D. G. 1982, MNRAS, 199, 883
Boccardi B., Krichbaum T. P., Bach U., Bremer M., Zensus J. A. 2016, A&A, 588, L9
Boccardi B., Perucho M., Casadio C., *et al.* 2021, A&A, 647, A67
Bonanno A., Urpin V. 2008, A&A, 480, 27
Bronzwaer T., Davelaar J., Younsi Z., *et al.* 2018, A&A, 613, A2
Bronzwaer T., Younsi Z., Davelaar J., Falcke H. 2020, A&A, 641, A126
Chatterjee K., Markoff S., Neilsen J., *et al.* 2020a, arXiv e-prints, arXiv:2011.08904
Chatterjee K., Younsi Z., Liska M., *et al.* 2020b, MNRAS, 499, 362
Davis S. W., Tchekhovskoy A. 2020, ARA&A, 58, annurev
De Villiers J.-P., Hawley J. F. 2003, ApJ, 592, 1060
Dexter J. 2016, MNRAS, 462, 115
Dexter J., Tchekhovskoy A., Jiménez-Rosales A., *et al.* 2020, MNRAS, 497, 4999
Dihingia I. K., Vaidya B., Fendt C. 2021, MNRAS, 505, 3596
Doeleman S. S., Fish V. L., Schenck D. E., *et al.* 2012, Science, 338, 355
Fanaroff B. L., Riley J. M. 1974, MNRAS, 167, 31P
Fender R., Gallo E. 2014, Space Sci. Rev., 183, 323
Fendt C. 2006, ApJ, 651, 272
Fernandes A. J., Garcia P. J., Lima J. J. 2012, Jets in Young Stellar Objects: Theory and Observations (Springer Science & Business Media)
Fishbone L. G., Moncrief V. 1976, ApJ, 207, 962
Gendre M. A., Best P. N., Wall J. V., Ker L. M. 2013, MNRAS, 430, 3086
Gold R., McKinney J. C., Johnson M. D., Doeleman S. S. 2017, ApJ, 837, 180
Han J. L. 2017, ARA&A, 55, 111
Hardee P., Mizuno Y., Nishikawa K.-I. 2007, Ap&SS, 311, 281
Igumenshchev I. V. 2008, ApJ, 677, 317
Inoue Y., Khangulyan D., Inoue S., Doi A. 2019, ApJ, 880, 40
Kagan D., Sironi L., Cerutti B., Giannios D. 2015, Space Sci. Rev., 191, 545
Kim J. Y., Krichbaum T. P., Lu R. S., *et al.* 2018, A&A, 616, A188
Komissarov S. S. 2004, MNRAS, 350, 427
Komissarov S. S., Barkov M. V., Vlahakis N., Königl A. 2007, MNRAS, 380, 51
Komissarov S. S., Barkov M. V. 2009, MNRAS, 397, 1153
Lyubarsky Y. 2009, ApJ, 698, 1570
Marshall M. D., Avara M. J., McKinney J. C. 2018, MNRAS, 478, 1837
McClintock J. E., Shafee R., Narayan R., *et al.* 2006, ApJ, 652, 518
McKinney J. C., Gammie C. F. 2004, ApJ, 611, 977
McKinney J. C., Tchekhovskoy A., Sadowski A., Narayan R. 2014, MNRAS, 441, 3177
Mingo B., Croston J. H., Hardcastle M. J., *et al.* 2019, MNRAS, 488, 2701
Mizuno Y., Fromm C. M., Younsi Z., *et al.* 2021, MNRAS, 506, 741

Mościbrodzka M. 2020, MNRAS, 491, 4807
Nakamura M., Asada K., Hada K., *et al.* 2018, ApJ, 868, 146
Narayan R., McClintock J. E. 2012, MNRAS, 419, L69
Nathanail A., Porth O., Rezzolla L. 2019, ApJ, 870, L20
Nathanail A., Fromm C. M., Porth O., *et al.* 2020, MNRAS, 495, 1549
Noble S. C., Krolik J. H., Schnittman J. D., Hawley J. F. 2011, ApJ, 743, 115
Novikov I. D., Thorne K. S. 1973, in Black Holes (Les Astres Occlus), 343
Olivares H., Porth O., Davelaar J., *et al.* 2019, A&A, 629, A61
Paczynski B., Bisnovatyi-Kogan G. 1981, Acta Astron., 31, 283
Penna R. F., Narayan R., Sadowski A. 2013, MNRAS, 436, 3741
Porth O., Olivares H., Mizuno Y., *et al.* 2017, Computational Astrophysics and Cosmology, 4, 1
Porth O., Chatterjee K., Narayan R., *et al.* 2019, ApJS, 243, 26
Porth O., Mizuno Y., Younsi Z., Fromm C. M. 2021, MNRAS, 502, 2023
Qian Q., Fendt C., Vourellis C. 2018, ApJ, 859, 28
Ressler S. M., Tchekhovskoy A., Quataert E., Chandra M., Gammie C. F., 2015, MNRAS, 454, 1848
Reynolds C. S. 2019, Nature Astronomy, 3, 41
Ripperda B., Bacchini F., Philippov A. 2020, arXiv e-prints, arXiv:2003.04330
Ryan B. R., Ressler S. M., Dolence J. C., Tchekhovskoy A., Gammie C., Quataert E., 2017, ApJ, 844, L24
Sádowski A., Narayan R., Penna R., Zhu Y. 2013, MNRAS, 436, 3856
Sádowski A., Wielgus M., Narayan R., *et al.* 2017, MNRAS, 466, 705
Shakura N. I., Sunyaev R. A. 1973, A&A, 500, 33
Sironi L., Spitkovsky A. 2014, ApJ, 783, L21
Sironi L., Petropoulou M., Giannios D. 2015, MNRAS, 450, 183
Spruit H. C., Foglizzo T., Stehle R. 1997, MNRAS, 288, 333
Stecker F. W., Done C., Salamon M. H., Sommers P. 1991, Phys. Rev. Lett., 66, 2697
Tchekhovskoy A., Narayan R., McKinney J. C. 2010, ApJ, 711, 50
Tchekhovskoy A., Narayan R., McKinney J. C. 2011, MNRAS, 418, L79
Tchekhovskoy A., Bromberg O. 2016, MNRAS, 461, L46
Tomimatsu A. 1994, PASJ, 46, 123
Vourellis C., Fendt C., Qian Q., Noble S. C. 2019, ApJ, 882, 2
Wold M., Lacy M., Armus L. 2007, A&A, 470, 531
Xie W., Lei W.-H., Zou Y.-C., *et al.* 2012, Research in Astronomy and Astrophysics, 12, 817
You B., Straub O., Czerny B., *et al.* 2016, ApJ, 821, 104
Younsi Z., Zhidenko A., Rezzolla L., Konoplya R., Mizuno Y. 2016, Phys. Rev. D, 94, 084025
Yuan F., Narayan, R. 2014, ARA&A, 52, 529
Zanni C., Ferrari A., Rosner R., Bodo G., Massaglia S. 2007, A&A, 469, 811
Zhang S. N., Cui W., Chen W. 1997, ApJ, 482, L155